Documenting Coherent Turbulent Structures in the Boundary Layer of Intense Hurricanes Through Wavelet Analysis on IWRAP and SAR Data

Devin E. Protzko, Stephen R. Guimond, Christopher R. Jackson, Joseph W. Sapp, *Senior Member, IEEE*, Zorana Jelenak, *Member, IEEE*, and Paul S. Chang, *Senior Member, IEEE*

***Abstract*— New radar remote sensing measurements of the turbulent hurricane boundary layer (HBL) are examined through analysis of airborne (Imaging Wind and Rain Airborne Profiler (IWRAP)) and spaceborne (synthetic aperture radar (SAR)) data from Hurricanes Dorian (2019) and Rita (2005). These two systems provide a wide range of storm intensities and intensity trends to examine the turbulent HBL. The central objective of the work is to document the characteristics of coherent turbulent structures (CTSs) found in the eyewall region of the HBL. Examination of the IWRAP data in Dorian shows that the peak, localized wind speeds are found inside the CTSs near the eye–eyewall interface. The peak winds are typically located at lower levels (0.15–0.50) km but sometimes are found at higher levels (1.0–1.5 km) when the CTSs are stretched vertically. A SAR overpass of Dorian's eyewall showed ocean surface backscatter perturbations at the eye–eyewall interface that have connections to the CTSs identified in the IWRAP data. Wavelet analysis, including detailed significance testing, was performed on the IWRAP and SAR data to study the CTS wavelengths and power characteristics. Both datasets showed a multiscale structure in the wavelet power spectrum with peaks at ∼10 km (eyewall), ∼4–5 km (merger of small-scale eddies), and ∼2 km (native scale of the CTSs). The ∼2-km native scale of the CTSs is robust across intensity trends (rapid intensification, weakening, and steady state), storm cases, and region of the storm. This information is useful for turbulence parameterization schemes used in numerical models that require the specification of a turbulent length scale.**

***Index Terms*— Boundary layer, hurricane, radar remote sensing, turbulence, wavelet analysis.**

Manuscript received 16 December 2022; revised 3 May 2023, 9 July 2023, and 6 August 2023; accepted 8 August 2023. Date of publication 18 August 2023; date of current version 8 September 2023. The work of Devin E. Protzko was supported by the University of Maryland Baltimore County (UMBC) Strategic Awards for Research Transitions (START) Grant to Stephen R. Guimond. The work of Stephen R. Guimond was supported by the Office of Naval Research (ONR) under Grant N00014-22-1-2078. The work of Joseph W. Sapp, Zorana Jelenak, and Paul S. Chang was supported by the National Oceanic and Atmospheric Administration Ocean Winds Program under Grant ST13301CQ0050/1332KP22FNEED0042. *(Devin E. Protzko and Stephen R. Guimond are co-first authors.) (Corresponding author: Stephen R. Guimond.)*

Devin E. Protzko was with the Physics Department and the Mathematics Department, University of Maryland Baltimore County, Baltimore, MD 21250 USA. He is now with the Johns Hopkins University Applied Physics Laboratory, Laurel, MD 20723 USA (e-mail: Devin.Protzko@jhuapl.edu).

Stephen R. Guimond was with the Physics Department, University of Maryland Baltimore County, Baltimore, MD 21250 USA, and also with the NASA Goddard Space Flight Center, Greenbelt, MD 20771 USA. He is now with the Department of Atmospheric and Planetary Sciences, Hampton University, Hampton, VA 23669 USA (e-mail: stephen.guimond@hamptonu.edu).

Christopher R. Jackson is with Global Ocean Associates, Alexandria, VA 22310 USA (e-mail: christopher.jackson@noaa.gov).

Joseph W. Sapp is with Global Science and Technology, Inc., Greenbelt, MD 20770 USA, and also with the National Oceanic and Atmospheric Administration, STAR Center for Satellite Applications and Research, College Park, MD 20740 USA (e-mail: joe.sapp@noaa.gov).

Zorana Jelenak is with the Cooperative Programs for the Advancement of Earth System Science (CPAESS), University Corporation for Atmospheric Research, Boulder, CO 80307 USA, and also with the National Oceanic and Atmospheric Administration, STAR Center for Satellite Applications and Research, College Park, MD 20740 USA (e-mail: zorana.jelenak@noaa.gov).

Paul S. Chang is with the National Oceanic and Atmospheric Administration, STAR Center for Satellite Applications and Research, College Park, MD 20740 USA (e-mail: paul.s.chang@noaa.gov).

Digital Object Identifier 10.1109/TGRS.2023.3305998

I. Introduction

THE hurricane is a warm-core system in approximate thermal wind balance, resulting in the maximum winds occurring in the lowest levels of the atmosphere. These intense winds interact with the ocean surface producing significant stress and a frictional boundary layer with a nearly logarithmic decrease in winds toward the surface in the mean (e.g., [6]). Typically, the vertical shear of the horizontal winds in the boundary layer draws energy from the mean flow (e.g., [5]) producing turbulent eddies with extreme winds of ∼80–100 m/s as indicated by in situ and remote sensing measurements [1], [8]. These turbulent eddies are responsible for direct wind damage to homes and infrastructure and play an important role in the storm intensification through their transport of moisture, momentum, and energy. Recently, Sroka and Guimond [18] showed that the turbulent eddies identified in Guimond et al. [8] can interact to produce regions of kinetic energy backscatter whereby the energy flows from small-scale waves to large-scale waves. This result is important because it provides a potential mechanism for intensification of the system that is not encoded in most turbulence parameterization schemes used in numerical models. However, the initial findings of [18] require more analysis to uncover the robustness of the results and to characterize additional aspects of the turbulent eddies across a range of storm intensities and intensity trends.

Through analysis of airborne radar and radiometer measurements in the most intense stages of Hurricane Rita (2005), Guimond et al. [8] showed the presence of coherent turbulent structures (CTSs) in the eyewall boundary layer with radial scales of ∼2 km. These features contained vertically coherent

signatures in the 3-D wind vector from the ocean surface through the full depth of the boundary layer and possibly higher. As a result, the CTSs can leave an imprint on the roughness of the ocean surface that can be detected from remote sensing instruments mounted on satellite and airborne platforms. In particular, satellite synthetic aperture radar (SAR) data detect this roughness imprint because the CTSs modulate the centimeter-scale capillary waves that are responsible for the radar backscatter from the ocean surface. Satellite SAR measurements have been providing very high resolution (∼100 m pixel spacing and lower) and wide swath views of mesoscale and microscale features at the ocean–atmosphere interface in hurricanes for many years. Previous studies have documented the structure of the eye, eye–eyewall interface, and boundary layer rolls [3], [10], [12], [20]. Zhang et al. [20] analyzed one SAR image of Hurricane Isidore (2002) and documented streak-like features with a dominant wavelength of ∼900 m. In situ data were collected from research aircraft in the boundary layer well outside of the eyewall and 24 h prior to the SAR overpass to understand the remote sensing measurements. They found good agreement between the wavelengths of the features seen in the SAR image and those analyzed from the in situ data. Li et al. [12] analyzed a SAR image of a hurricane and found the presence of ∼2–3-km wavelength features in the far outer regions of the storm that they attributed to boundary layer rolls.

Despite the studies described above, there is much to be learned about the turbulent structures found in the boundary layer and ocean–atmosphere interface in hurricanes from both a scientific and remote sensing perspective. On the scientific side, more detailed information on the circulation signatures, momentum fluxes, and role of the eddies in the mean system evolution is needed. On the remote sensing side, the interpretation of the wind structures producing the SAR backscatter can be complicated and ambiguous, which requires ancillary data sources to provide independent information on the 3-D wind vector. Wind measurements of the turbulent hurricane boundary layer (HBL) have been largely limited to Lagrangian point samples from dropsondes and sporadic (noncolumnar) flight-level data. While valuable sources of information, these data cannot provide the localized structure of the HBL at high resolution and require gathering data over many hours and many storms to compile a complete, averaged picture of this layer. However, new algorithms and processing of data from the Imaging Wind and Rain Airborne Profiler (IWRAP) airborne Doppler radar can provide the 3-D wind vector over the HBL at a grid spacing that is fully capable of resolving large turbulent eddies [7], [9].

The main goal of the present work is to characterize CTSs in a new set of IWRAP measurements collected over the course of several days in Hurricane Dorian (2019). Furthermore, using additional data from Hurricane Rita (2005), wavelet analysis is used to extract the localized wavelengths of turbulent eddies in both IWRAP and satellite SAR data to examine their similarities and differences. The IWRAP data are used to help interpret the SAR imagery of the ocean/atmosphere interface and suggest ways to combine the two data sources to make inferences about the role of turbulence in the storm dynamics.

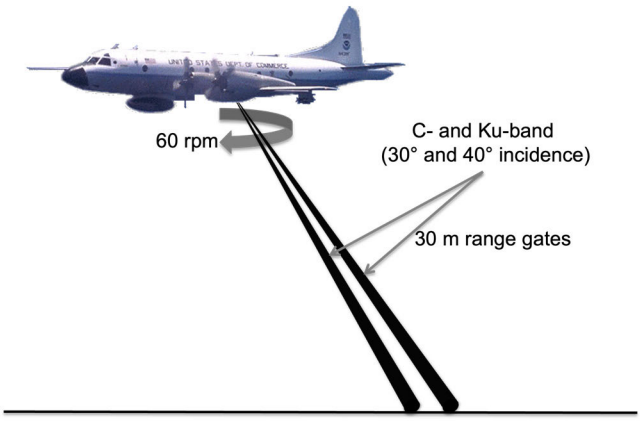

Fig. 1. Measurement geometry of the conically scanning IWRAP instrument on the NOAA WP-3D aircraft. Note that the specified incidence angles are examples and have changed through the years of IWRAP flight experiments.

However, the kinematic signatures of the CTSs as well as their detailed dynamics are not addressed in this study.

II. Data Sources and Storm Cases

A. IWRAP

The IWRAP is a downward-pointing, dual-frequency (C- and Ku-band), dual-polarization airborne Doppler radar that measures surface backscatter and volume reflectivity/Doppler velocity from precipitation at 30-m range resolution. Typically, both radars have been conically scanned pencil beams at two simultaneous incidence angles via a phased array antenna, but in Hurricane Dorian (2019), the C-band radar operated with a statically mounted fanbeam antenna on loan from ESA [16], [17]. The Ku-band incidence angles can be adjusted from ∼20° to 50° off-nadir, but for this study, we focus on the Ku-band, inner beam data with a calibrated, nominal incidence angle of ∼25°. This incidence angle allows wind retrievals down to ∼150–200 m height above the ocean surface.

The IWRAP is mounted on the NOAA WP-3D (P-3) research aircraft and routinely samples extreme wind regions of tropical and extratropical systems by flying radial transects through the storm center. The P-3 aircraft has a typical airspeed of ∼125 m/s and a flight altitude of ∼1.5–2.5 km. With the inner beam data analyzed here, the swath width at the ocean surface is ∼2 km. More detailed information on the IWRAP system can be found in Fernandez et al. (2005) [4]. Fig. 1 shows a concept diagram of the measurement geometry of the IWRAP instrument on the P-3 aircraft.

The IWRAP scans at 60 r/min allowing wind retrievals with up to 125-m horizontal and 30-m vertical grid spacing. Calculations of the three Cartesian wind components (3-D winds) over the full IWRAP sampling volume are computed following the variational algorithm described in [7]. The IWRAP 3-D winds have been thoroughly validated and compared very well with in situ flight-level data [7], G18. Guimond et al. [9] designed an IWRAP 3-D winds simulator using a large eddy simulation of a hurricane and found from spectral analysis that the 3-D winds are fully resolved at 4–5 Δx, where Δx is the

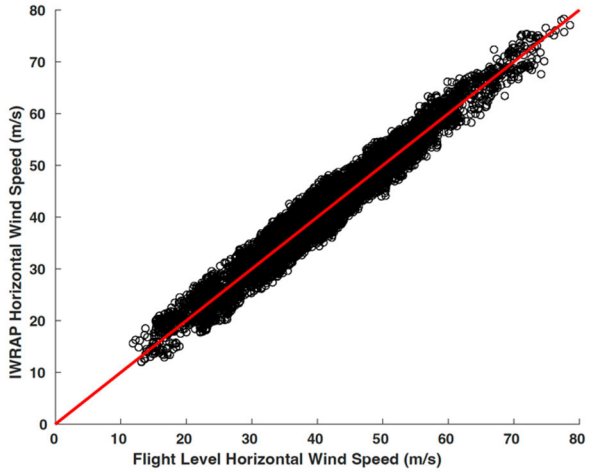

Fig. 2. Validation of IWRAP computed horizontal wind speed closest to the aircraft with flight-level horizontal wind speed for all data collected in Hurricane Dorian (2019). See the text for details of the statistics.

retrieval grid spacing. This means that with a grid spacing of 125 m, the IWRAP 3-D winds can capture the full essence of turbulent eddies with scales of ∼600 m.

In this work, we utilize data from flights into Hurricane Rita (2005) and Hurricane Dorian (2019), which had high-quality signal-to-noise ratio (SNR) performance in precipitation. Note that some regions of data have been removed because the quality was not sufficient due to attenuation of the Ku-band signal in intense precipitation. These regions will be described in the results where appropriate. The Rita and Dorian 3-D winds are processed at 250- and 125-m horizontal grid spacing, respectively, with 30-m vertical spacing. Fig. 2 shows the validation of the IWRAP computed horizontal wind speed closest to the aircraft with flight-level data for the Hurricane Dorian (2019) case. The validation statistics indicate a root-mean-square error (RMSE) of 2.32 m/s, a relative RMSE of ∼5%, and a correlation coefficient of 0.97 for a total of ∼15 000 points. These statistics are similar to previously published studies [8].

B. SAR

SAR, such as other microwave sensors, works by transmitting a radar pulse and recording the backscatter energy from the reflected pulse. The SAR records both the amplitude and phase of the return signal and achieves the "synthetic aperture" by combining successive return pulses over a finite integration time. This allows the resulting SAR image to achieve a spatial resolution in the along-track direction comparable to that obtained in the range direction (on the order of tens of meters). Scatterometers, real aperture radars, and classically processed altimeters are limited in their along-track resolution (on the order of kilometers) by the size of the antenna beam pattern.

In this article, C-band SAR imagery from Hurricane Rita (2005) and Hurricane Dorian (2019) is analyzed. Imagery from Rita was acquired by the advanced SAR (ASAR) that was on board the European Space Agency's (ESAs) ENVISAT satellite (2002–2012), with the Dorian imagery acquired by ESAs Sentinel-1B SAR system (since 2016). The collection

TABLE I
SAR MEASUREMENTS ANALYZED IN THIS STUDY

Hurricane	Date	Sensor / Mode	Swath / Resolution	Polarization	V_{max}	R_{max}
Rita	22 Sept 2005	ASAR Wide Swath	400 km / 150 m	VV	*79.7 m/s	N/A
Dorian	29 Aug 2019	S1B Extended Wide	400 km / 80 m	VV, VH	37.6 m/s	9.3 km
Dorian	04 Sept 2019	S1B Interferometric Wide	240 km / 40 m	VV, VH	*46.3 m/s	N/A

parameters are presented in Table I. Each acquisition was acquired in a "wide swath" mode by which multiple beam positions are combined to achieve a swath width larger than any individual beam. These wide swath images are beneficial for obtaining data over hurricanes, which can extend for hundreds of kilometers in diameter. In addition, while all images were acquired with vertical transmit/vertical receive or VV polarization (i.e., co-polarization channel), Sentinel-1B also acquired the corresponding cross-polarization channel (vertical transmit/horizontal receive or VH). The two Dorian SAR images analyzed in this article utilize the VH channel. The native SAR pixel spacing is listed in Table I, but in postprocessing, these pixels are interpolated to a grid that is consistent with the IWRAP data (250 m for Rita and 125 m for Dorian). Then, the SAR data are filtered to the fully resolved scale of the IWRAP data, which is ∼1000 m for Rita and ∼600 m for Dorian. This filtering eliminates all small-scale noise in the native SAR data, but the noise power was also removed before this postprocessing. All postprocessing is performed in linear units.

Furthermore, Table I lists the values of the maximum winds (V_{max}) computed from SAR wind retrievals. When SAR winds are not available in the eyewall, best track values from the National Hurricane Center (NHC), denoted by an asterisk in Table I, are listed. The radius of maximum winds (RMWs) denoted R_{max} is also listed where it is available from the SAR data and not available ("N/A") from the best track dataset.

The images used in the analysis are multilook (detected) ground range. This means that there has been some averaging in both the range and along-track (azimuth) directions to reduce the image noise and the data have been projected into the ground range. The principal measurement from SAR is the normalized radar cross section (NRCS). The NRCS is the conventional measure of the strength of a reflected radar signal in the horizontal plane. It is a dimensionless number usually expressed on a decibel scale (dB) representing the ratio of the observed power from the scattering surface to that of the expected return power from a surface with a 1-m^2 area. In general, the NRCS is dependent on incidence angle, polarization, wind speed, and wind direction. This dependence is used to construct empirical relationships, called geophysical model functions or GMFs, between the NRCS, polarization, viewing geometry, and geophysical parameters (wind speed and direction). The focus of this article is on the calibrated NRCS measurement, due to difficulties and uncertainties inherent in wind vector retrieval as well as

the larger spatial scale these retrievals represent (∼3 km). By analyzing the spatial variability of the NRCS over a fixed polarization and viewing geometry, this variability can be related to wind speed.

Radial sections of data are selected from the SAR images for analysis in Section IV. These selected radials contain NRCS variability from two sources: geophysical variability associated with the wind vector and instrument variability (relative azimuth and incidence angle effects). The instrument variability was estimated by computing the NRCS over the incidence angle ranges contained within the radials for fixed wind speeds. The relative azimuth effects for these radials are very small and can be neglected. The NRCS tests showed small effects (a maximum of ∼0.25 dB across the full radial range) from incidence angle changes. Translating this number to the scales considered in the wavelet analysis (1–5 km, for the most part), there is a 0.036- and 0.007-dB incidence angle contribution for the 5- and 1-km scales, respectively. The perturbation NRCS data show oscillations of at least ∼1.0 dB for the 5-km scales and ∼0.5 dB for the 1-km scales. Thus, the SNR is very large ($\gg$1) and the incidence angle effect on the CTS signal is negligible.

Precipitation can affect the NRCS measurement from three primary processes: 1) raindrops producing capillary and gravity-capillary waves that can interact with the radar signal; 2) attenuation from precipitation integrated along the beam path; and 3) volume scattering from precipitation. The focus of this study is on the intense winds associated with hurricanes and the effect from 1) is likely small (e.g., [2]). In the core of the eyewall, intense rain can produce attenuation of the radar signal, but for the C-band SAR data analyzed here, this effect should be minimized, but still possible in isolated regions. Finally, as described in Section IV, many of the prominent CTSs are found at the eye–eyewall interface, which is located radially inward (∼5 km) from the maximum precipitation in the center of the eyewall. Thus, the effects from attenuation and volume scattering on the NRCS will be reduced in this region, but still present to some degree. Furthermore, it is important to note that wind and rain are generally highly correlated variables in a hurricane because latent heat release is what drives the dynamics. Thus, the coupled wind and rain effect in the NRCS is still valuable to analyze because the CTSs under examination carry both of these signatures.

C. Storm Cases

Radar data from IWRAP and SAR measurements are analyzed for two intense storm systems: Hurricane Rita (2005) and Hurricane Dorian (2019). The IWRAP data for Rita were collected on September 22 and 23 between 1800 and 2200 UTC each day, while the SAR overpass of the storm occurred earlier in the day on September 22 at 0345 UTC. During this time period, Rita was a very powerful category five system with maximum sustained winds of ∼80 m/s and a minimum central pressure of 897 hPa at ∼0600 UTC 22 September. Later in the day on 22 September, Rita encountered stronger vertical wind shear and was undergoing an eyewall replacement cycle, which resulted in a steady weakening trend. The IWRAP data for Dorian analyzed here were collected on the following dates and times: August 31 between 1400 and 1430 UTC, September 3 at 0020 and 0950 UTC, September 4 at 2150 UTC, and September 5 at 0100 UTC. The SAR overpasses of the storm occurred on August 29 at 1021 UTC and September 4 at 1108 UTC. The first SAR overpass occurred ∼52 h before the closest IWRAP sample, while the second overpass occurred ∼11 h before the closest IWRAP sample. The methodology for evaluating these two datasets is described in Section III. The IWRAP and SAR data for Dorian cover a very wide range of storm intensities. On August 29, the system was classified as a hurricane with a steady intensification trend, and then on August 31, Dorian was in the midst of a rapid intensification phase with a major hurricane classification. The system reached peak intensity just before September 2 and then entered a fairly rapid weakening phase on September 3 and 4 where it was downgraded to a hurricane classification. Finally, on September 5, the storm increased intensity slightly to regain major hurricane status for a brief period of time.

III. Methodology

A. Statistical Sampling Approach

It is difficult to get an exact match up in time and space between a SAR overpass and an IWRAP flight given the limited sampling of both instruments. The SAR data provide excellent spatial coverage of systems at the cost of poor temporal coverage, while IWRAP data can provide much better temporal coverage with limited spatial coverage. To circumvent these sampling issues, a statistical methodology is adopted for comparison purposes. The premise is to gather statistics of the eddy features in both SAR and IWRAP data and then compare the parameters of these distributions such as the mean/variance and shape of the probability density function. The advantage of the SAR data is the high resolution over a very large domain, while the IWRAP data provide accurate 3-D winds in the HBL. The statistical comparisons of the two datasets can be used to make inferences on the spatial coverage of the eddies and their potential role in the storm evolution.

It is important to construct a common sample size in both SAR and IWRAP data to enable a meaningful statistical comparison. Naturally, there are differences in the spatial coverage, resolution, and other properties of the measurements, so the following procedure was performed. The SAR NRCS data are interpolated to a storm-centered cylindrical grid with 1.0° azimuthal spacing and a radial spacing that is consistent with the respective IWRAP 3-D winds grid spacing for each storm analyzed. The flight tracks of the P-3 aircraft are typically radials from the storm center and the IWRAP wind fields at nadir are pulled out for comparison to the SAR data. The storm centers for all data shown in this work are determined from aircraft center fixes interpolated to the appropriate time.

For the Rita case, there were five total IWRAP passes of sufficient quality on 22/23 September covering the time interval ∼1800–2200 UTC each day. The SAR image for Rita was collected on 22 September, but at 0345 UTC. Five radials

were extracted from the SAR image on the cylindrical grid to match the sample size of IWRAP. The same procedure is applied to the Dorian case, except six-quality IWRAP passes covering several days and times were found (31 August 1400 and 1430 UTC, 3 September 0020 and 0950 UTC, 4 September 2150 UTC, and 5 September 0100 UTC). There were two quality SAR images for the Dorian case with one on 29 August 2019 at 1021 UTC and one on 4 September 2019 at 1109 UTC. Three radials were extracted from each SAR image to match the sample size in the IWRAP data. With the above processing of the two datasets to a common sample size, wavelet analysis can be performed.

B. Wavelet Analysis

Wavelet analysis is a method for processing a complicated signal and extracting information on the fundamental properties of that signal (amplitude, phase, wavelength, frequency, or wavenumber) and how those properties evolve in time or space. A Fourier transform also decomposes a signal into these fundamental wave properties, but it does not provide information on when (time) or where (space) these waves are found. In this sense, the Fourier transform provides "bulk" wave characteristics of the input signal, while wavelets provide "localized" wave characteristics through a convolution operation. Localized signal processing is very useful for characterizing and understanding turbulent features present in the HBL as measured from remote sensing datasets and placing them into context with the larger scale vortex.

The common SAR and IWRAP samples described in the previous subsection are processed with a continuous wavelet transform using a Morlet mother wavelet following the methodology of [19]. The Morlet wavelet was chosen for its high time/space resolution (several positive/negative oscillations in physical space) and smooth depiction of power (the oscillations get merged together during the convolution), which helps in physical interpretation. In addition, the wavelet scale and Fourier scale are essentially equivalent to the Morlet mother wavelet, which allows for ease of interpretation of the physical scale of the turbulent features.

Before feeding the SAR and IWRAP samples into the wavelet transform, we extract 1-D (radial) signals from the two datasets. This is trivial for the SAR data as we have already selected radials from the horizontal images. For the nadir IWRAP data, a function of radius and height, the lowest height levels of quality data present in the IWRAP passes are averaged. The lowest levels for the Rita and Dorian IWRAP data are 150–200 m above the ocean surface. However, attenuation of the Ku-band signal can be significant in some patchy regions of the lower boundary layer, which is mainly an issue for the Dorian data. Detailed figures illustrating this behavior will be presented in Section IV when the results are discussed.

The gaps in data coverage resulting from attenuation can affect the ability to perform a seamless wavelet analysis. To avoid the attenuated regions, the nadir IWRAP data are averaged over the 0.50–0.75-km height range for some Dorian passes and over the 0.25–0.50-km height range for some Rita passes. Passes that have minimal attenuation are averaged over the ~0.18–0.50 height range. Markings are shown on the IWRAP Dorian images in Section IV to denote the layer used for further processing.

The differences in the height range do not make a significant difference in the results because the features examined here are vertically coherent over these intervals. Regions with small gaps after vertically averaging are filled with linear interpolation to provide a continuous signal for the wavelet analysis. These small regions are not noticeable in the resulting wavelet image and do not affect the results of this article. However, sometimes the data gaps are large where there is no volume scattering from precipitation. These regions are still filled with linear interpolation, but they are not considered in the resulting analysis (denoted by a "cutoff radius"). Markings are shown on the IWRAP Dorian images in Section IV to denote the location of the cutoff radii.

Using these radial signals from each dataset, scales greater than ~5 km are removed by applying a filter to the data and subtracting this from the total fields to get a perturbation field. The filtering above 5 km is applied because the focus of this study is on the smaller scale turbulent features in the HBL, and Guimond et al. [8] found that scales above 5 km are outside the range of eddy wavelengths for the Rita IWRAP data. However, the filter that is employed (boxcar with forward and backward applications to eliminate phase shifts) does not cleanly separate the scales at a 5-km wavelength. Instead, some energy just upscale from the 5-km wavelength creeps into the perturbation signal that is processed through the wavelet transform. This does not affect the analysis or interpretation of the eddy scales, but the extra power is visible in the wavelet images. It is useful to show this power above a scale of 5 km to provide context for the information at smaller scales. This is especially true in the eyewall, where a superposition of scales is present (convective and eddy scales).

Before proceeding with the wavelet transform, the signal is padded with zeros to increase the number of points up to the next higher power of 2, which significantly reduces the edge effects [19]. Edge effects are still possible, and they are marked on the wavelet images with the "cone of influence" or COI. Data outside the lines denoted as the COI are subject to larger uncertainty. These edge effects are not a concern at far radii in the signals because this region does not usually contain important information on eddies. However, at near radii in the eyewall region, edge effects could potentially obscure the interpretation of the wavelet analysis.

To address the edge effects and include data outside the COI in the scientific analysis, detailed significance testing was performed following Torrence and Compo [19] and Zhang and Moore [21]. This significance testing procedure allows confidence levels to be associated with data anywhere within the wavelet image for further physical interpretation. The perturbation IWRAP and SAR data were found to be mostly normally distributed, and thus, the significance tests outlined in Torrence and Compo [19] are applicable.

First, the perturbation IWRAP and SAR data are normalized (zero mean and unit standard deviation) before the wavelet analysis and significance testing are performed: $Y = (X - \bar{X})/\sigma(X)$, where X is the input signal, the overbar

is the mean, and σ is the standard deviation. Next, the normalized data are fit to the AR1 (lag-1 autoregressive with Gaussian white noise) model described in Torrence and Compo [19, eq. (15)] to estimate the lag-1 coefficient and standard deviation parameters of the model. The data fits to the model are performed with a maximum likelihood approach. The lag-1 coefficient is used to determine the 95% confidence level for a red-noise process following the methodology in Torrence and Compo [19].

To establish a robust confidence level outside the COI, the Monte Carlo test described in Zhang and Moore [21] is employed. The AR1 model parameters determined from the data record are used to generate 100 random ensemble members to the left and right of the normalized input data with the same size. This procedure produces 100 individual signals with a length of three times the original data. Each individual signal is fed into the wavelet processing and significance testing. The resulting arrays are averaged over the ensemble members (note that the original signal in the middle does not change with this averaging). The averaged power (P, dimensionless) is divided by the wavelet scale to remove the bias inherent to larger wavelengths using the Torrence and Compo [19] methodology [13], $P = |W_n(s)|^2/s$, where $W_n(s)$ is the complex wavelet transform for localized spatial index n and wavelet scale s. Finally, the padding surrounding the original data is clipped. The above procedure allows data anywhere in the wavelet image to be included in the histograms and physically interpreted at the 95% confidence level.

The wavelengths of dominant turbulent features are selected from the wavelet images subject to the following constraints: 1) 95% confidence level anywhere within the wavelet image; 2) wavelength less than or equal to 5 km and greater than 1 km; and 3) radius less than the cutoff. The cutoff radius is the start of large, interpolated regions. Points that meet all of these thresholds are aggregated into histograms for each dataset (IWRAP and SAR) and stratified by the inner core ($r* <= 1.5$) and outer core ($r* > 1.5$), where $r* = r/\text{RMW}$. Note that the CTSs are not pure sine waves, and thus, they will project onto a band of wavelengths and radii about the center of the features. The goal with the histograms is to count this "footprint" of wavelengths associated with the CTSs.

The procedure described above to build histograms is done exactly the same for the IWRAP and SAR data. However, for the SAR data, the focus is on the NRCS, which is directly related to the horizontal wind stress. For the IWRAP data, the focus is on the computed horizontal wind speed.

IV. Results

A. Case Study of Hurricane Dorian (2019)

For the case study of Dorian, wavelet analyses are based on the IWRAP and SAR sampling times in Fig. 3, which shows a comparison of wind speeds gathered from SAR, IWRAP, and NHC best track data. Overall, there is good agreement between the different forms of data, but the IWRAP estimates are consistently higher, especially on 5 September. This is likely due to the near instantaneous, very high-resolution nature of the IWRAP data, and the definition of "maximum" relative to the NHC estimates.

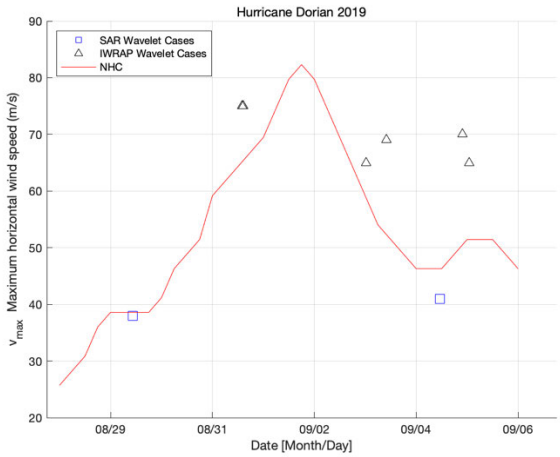

Fig. 3. Time series of maximum sustained wind speed (m/s) for Hurricane Dorian (2019) produced by the NHC. Overlaid on top of the time series are maximum wind speed estimates from SAR data (squares) and IWRAP data (triangles). Wavelet analyses for Dorian are based on these overlaid data sources.

Fig. 4 shows nadir vertical cross sections of IWRAP horizontal wind speed on 31 August at 1400 and 1430 UTC. During this time period, the storm was in a rapidly intensifying state located East of the Bahamas. The maximum wind speed is ~75 m/s in both panels located at radius (r)/height (z) = ~17/1.60 km at 1400 UTC and ~20/0.27 km at 1430 UTC. Attenuation below ~0.5 km height for $r < 20$ km at 1400 UTC may remove higher wind speeds, but the narrowing of the high wind speed column at $r \sim 17$ km from the top edge of the data down to $z = 0.5$ km suggests that this is unlikely. The region of high wind speeds located at the upper regions of the data is likely due to strong updrafts from turbulent eddies in the eyewall transporting high momentum air upward. The high wind speed columns in Fig. 4 are narrow, perhaps 5 km or more in the radial dimension, with smaller scale eddy features located radially inward, outward, and within the larger column. The black arrows point to examples of discrete eddies. The red marks on the height axis highlight the layer of IWRAP data that are used to perform the wavelet analysis. The black vertical line marks the cutoff radius used to truncate the wavelet analysis when building the histograms. Other IWRAP figures show similar markings and are not repeated in the text.

The corresponding wavelet images for these two radial legs are shown in Fig. 5. The white contour highlights the 95% confidence level used to build the CTS wavelength histograms. The vertical gray line marks the cutoff radius used to truncate the wavelet analysis when building the histograms, which corresponds to the black vertical line in Fig. 4. All other wavelet images follow these markings, and thus, the description is not repeated in the text. The wavelet image on 31 August at 1400 UTC (IWRAP data are averaged between 0.50 and 0.75 km height) shows that the peak power (~6) is located near $r = 15$ km, which is close to the RMW. Multiple peaks in the power are visible at ~7-, ~3-, and ~1-km wavelengths,

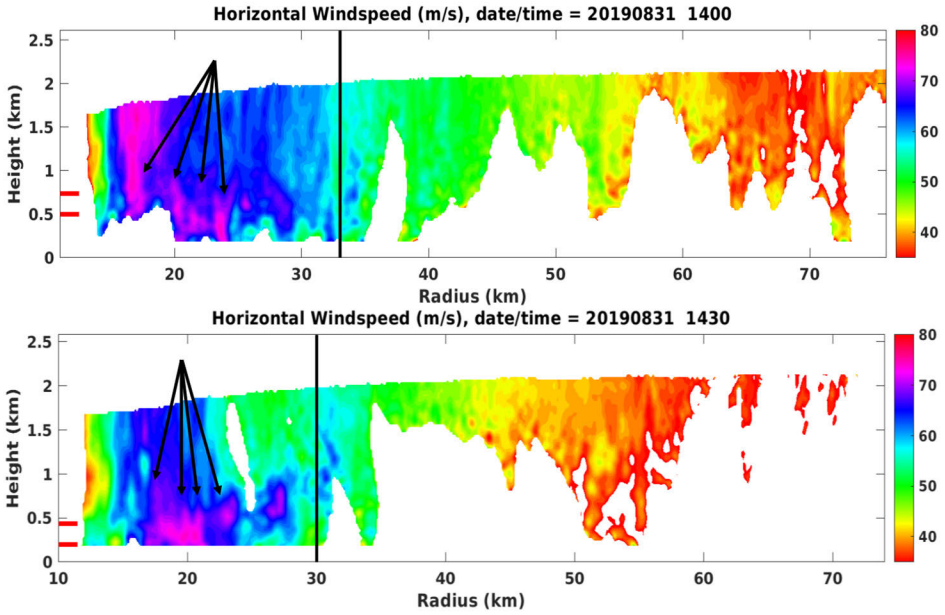

Fig. 4. IWRAP nadir vertical cross sections of wind speed in Hurricane Dorian (2019) on 31 August at (top) 1400 UTC and (bottom) 1430 UTC. The black arrows point to examples of discrete eddies. The red marks on the height axis highlight the layer of IWRAP data used to perform wavelet analysis. The black vertical line marks the cutoff radius used to truncate the wavelet analysis when building the histograms.

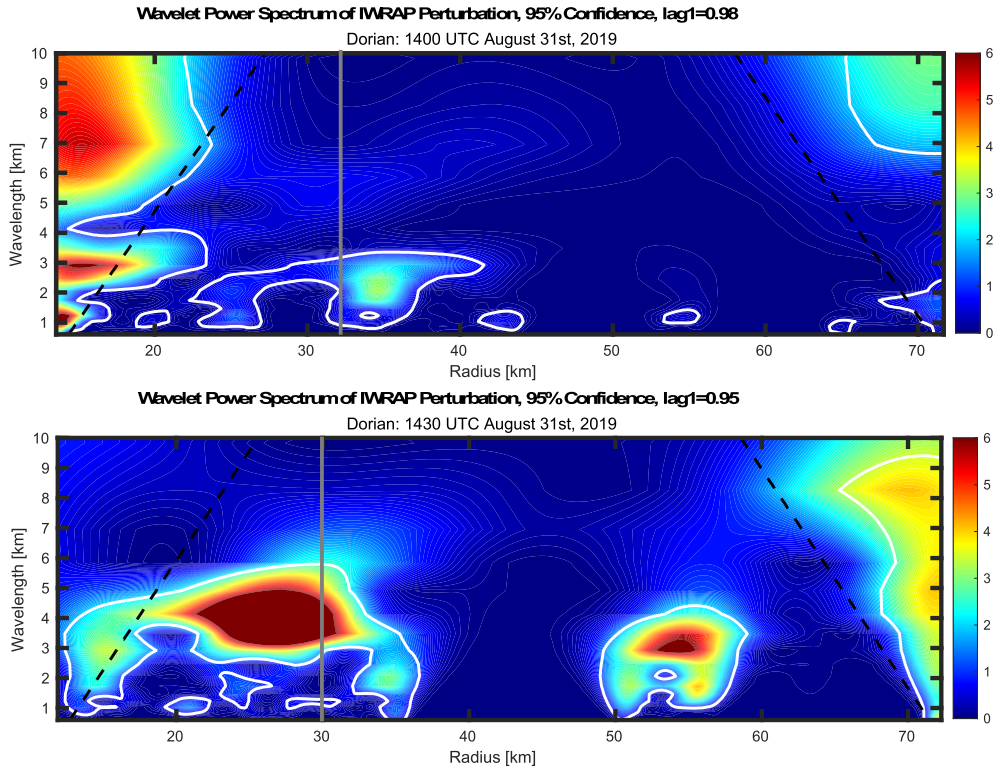

Fig. 5. Wavelet images corresponding to the IWRAP Dorian wind speed data shown in Fig. 4 on 31 August at (top) 1400 UTC and (bottom) 1430 UTC. The colors show normalized power as defined in the text. White lines denote the 95% confidence level used to build the histograms and the black dashed lines denote the COI. The estimated lag-1 coefficient used in the significance testing is listed above each wavelet image. The vertical gray line marks the cutoff radius used to truncate the wavelet analysis when building the histograms.

which are all statistically significant at the 95% level. This distribution of power reflects the multiscale nature of the turbulent structures in the heart of the eyewall with a superposition of large-scale features (scales $>$ 5 km) that likely have a convective origin to small-scale features (scales 1–3 km) that may have a mixture of shear and convective driven origins. Additional significant peaks in power can be seen around $r = 25$ km associated with eddy wavelengths of 1–2 km. The larger power value of $\sim$4 at $r = 35$ km is likely not physical due to a gap in data at this location.

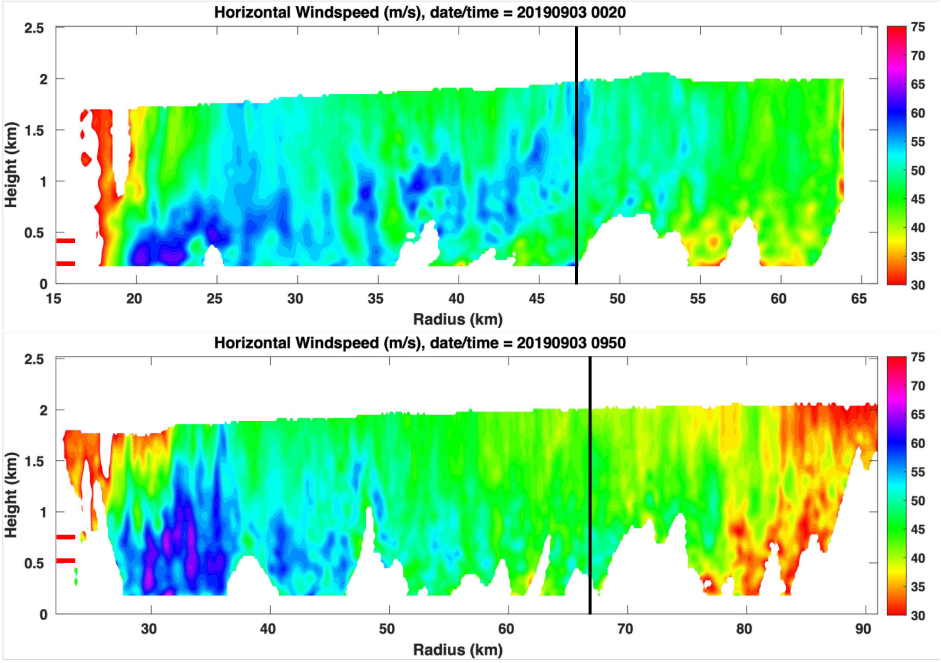

Fig. 6. IWRAP nadir vertical cross sections of wind speed in Hurricane Dorian (2019) on 3 September at (top) 0020 UTC and (bottom) 0950 UTC. All other shown markings are the same as in Fig. 4.

The wavelet image on 31 August at 1430 UTC (IWRAP data are averaged between 0.18 and 0.50 km) shows a dominant region of power (>6) between $r = 20$ and 30 km associated with intense, discrete eddies visible in the wind speed image (see Fig. 4) at around 0.5 km height. The wavelengths connected with the peak power span the range of ∼3–5 km with the center at ∼4 km. Weaker regions of significant power are present in this same radial band with scales of 1–2 km, which is consistent with a multiscale structure in the eyewall. There are large gaps in the IWRAP data beyond $r = 30$ km and we do not interpret the wavelet image in this region.

Fig. 6 shows the nadir vertical cross sections of IWRAP wind speed on 3 September 0020 and 0950 UTC, during a weakening trend of the storm located off the East coast of Florida. The maximum wind speeds are ∼65 and ∼69 m/s and are located at $r = 22$ km/$z = 0.25$ km and $r = 31$ km/$z = 0.18$ km at 0020 UTC and 0950 UTC, respectively. During the 0020 UTC leg, the strongest winds are very shallow, located at or below 0.50 km height with isolated turbulent eddies with stronger winds extending out to ∼50 km radius. During the 0950 UTC leg, the maximum winds are occurring in thin, turbulent filaments located in the eyewall and at the inner edge of the eyewall. These features extend from the lowest level of data (0.18 km) up to ∼1.00–1.75 km height with an increase in height moving radially outward. For reference, the peak radar reflectivity and associated rain rate (not shown) is located at $r = 37$ km where attenuation is observed at lower levels in Fig. 6 at 0950 UTC. Thus, the peak precipitation is located ∼5 km radially outward from the CTSs located at the eye/eyewall interface. This displacement between the maximum winds associated with the CTSs and the maximum precipitation has implications for the SAR NRCS measurements discussed later.

The corresponding wavelet images for these two radial legs are shown in Fig. 7. Relative to the previous wavelet power on 31 August (see Fig. 5), the power on 3 September 0020 UTC is significantly weaker with only a small region of power (∼6) at $r = 35$ km. At this radius, a distinct, tall eddy can be seen in the IWRAP image (see Fig. 6) extending from ∼0.18 to ∼1.25 km height. The wavelet image shows that this eddy has a wavelength centered near 3 km. Near the RMW (22 km), the power is weaker but a local, significant maximum of around 3.5 can be seen at this radius with a wavelength of ∼1.5 km, which is connected to the eddies in the IWRAP image below 0.5 km height in Fig. 6. Note that the IWRAP data are averaged between 0.18 and 0.50 km for this radial leg. The wavelet power has larger values (>6) on 3 September 0950 UTC in a band between ∼40 and 50 km radius. This band is associated with more isolated eddies just outside of the RMW region with scales of ∼5 km. Near the RMW (∼31 km), the thin, turbulent filaments present in the IWRAP image (see Fig. 6) have power values of ∼5 with wavelengths centered around 2 km. The IWRAP data are averaged between ∼0.5 and 0.75 km for this leg to avoid some attenuated regions.

Fig. 8 shows the nadir vertical cross sections of IWRAP wind speed on 4 September at 2150 UTC and 5 September at 0100 UTC, during a slight reintensification phase of the system off the Southeastern coast of Georgia. There is an interesting similarity between the eyewall boundary layer structure on 3 September at 0950 UTC (see Fig. 6) and that on 4 September at 2150 UTC (see Fig. 8). Both radial legs of data show thin, turbulent features at the eye/eyewall interface, but those on 4 September at 2150 UTC are stronger and extend higher in altitude, up to nearly 2 km height, when compared to the turbulent eddies on 3 September at 0950 UTC. While there are several possible reasons for the higher vertical extent

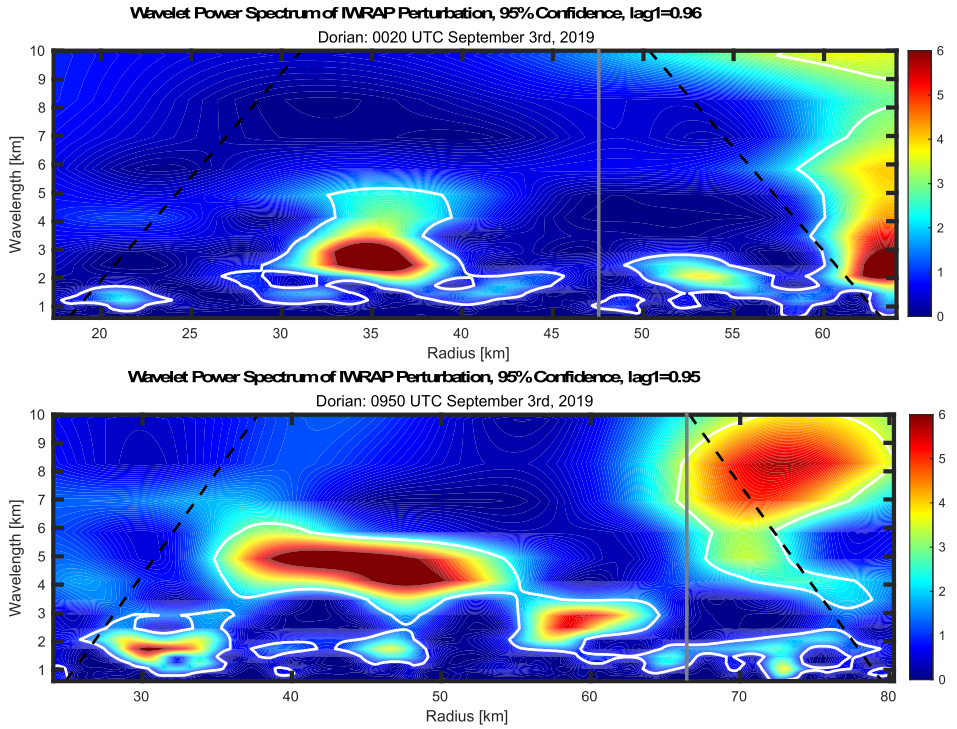

Fig. 7. Wavelet images corresponding to the IWRAP Dorian wind speed data shown in Fig. 6 on 3 September at (top) 0020 UTC and (bottom) 0950 UTC. All other shown markings are the same as in Fig. 5.

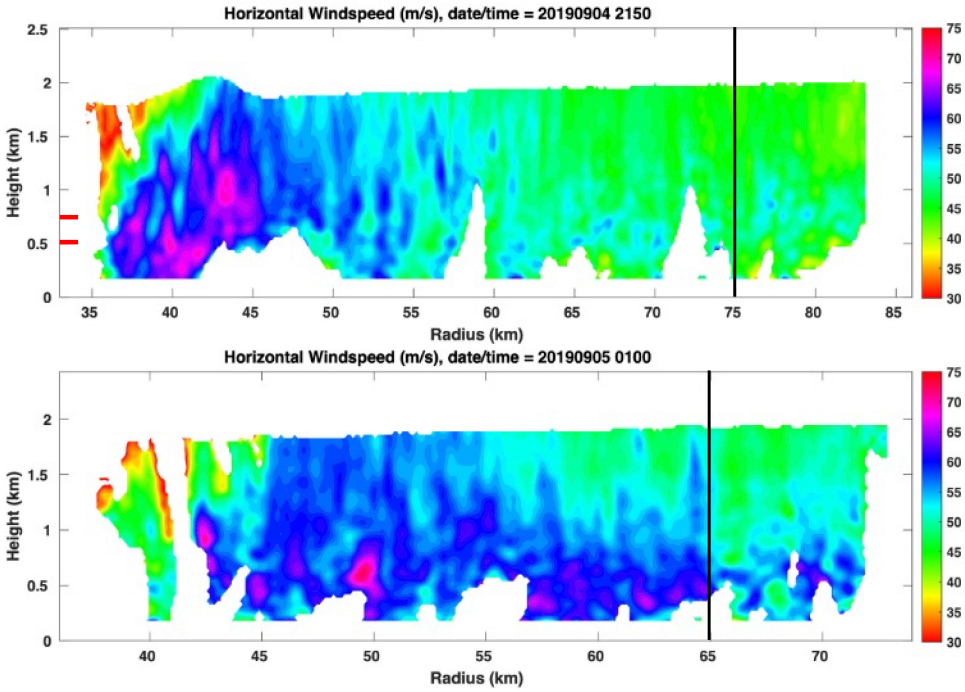

Fig. 8. IWRAP nadir vertical cross sections of wind speed in Hurricane Dorian (2019) on (top) 4 September at 2150 UTC and (bottom) 5 September at 0100 UTC. All other shown markings are the same as in Fig. 4.

of turbulent features on the 4 September 2150 UTC pass, the reintensification phase is likely connected to convective activity, which can stretch and accelerate the flow in these regions. The maximum winds are again occurring within these eddies with a value of ~70 m/s located at r = ~40 km/z = 0.5 km. Similar values are also found at ~1 km height near r = 43 km, illustrating the potential ability of the eddies to transport high momentum air aloft. The maximum precipitation, shown by the region of missing data due to strong attenuation, is centered around r = 46 km. Thus, the peak precipitation in the eyewall is out of phase with the maximum wind speed occurring within the CTSs at the

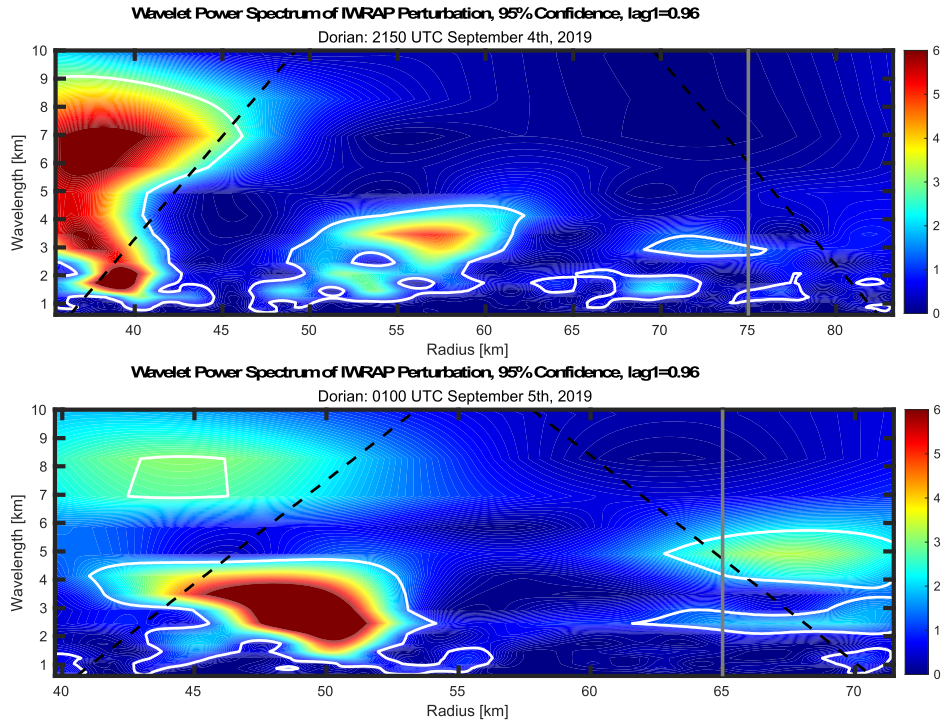

Fig. 9. Wavelet images corresponding to the IWRAP Dorian wind speed data shown in Fig. 8 on (top) 4 September at 2150 UTC and (bottom) 5 September at 0100 UTC. All other shown markings are the same as in Fig. 5.

eye/eyewall interface by about 5 km. This displacement is similar to other radial legs (Fig. 6, 0950 UTC).

The radial leg on 5 September at 0100 UTC does not show a concentration of higher winds in the eyewall as observed in most of the previous data. The turbulence structure is more scattered and spread out to larger radii (∼65 km) with most of the largest wind values occurring at or below 0.5 km height with values near ∼65 m/s.

The wavelet images for these radial legs are shown in Fig. 9. In the 4 September 2150 UTC pass (IWRAP data averaged between 0.50 and 0.75 km height), a wide range of energetic length scales are present in the range $r = 35$–40 km with elevated power values from ∼5 to >6 visible. The dominant power is centered over three distinct wavelength peaks: 6–7, 3–4, and ∼2 km. This multiscale structure located at the eye/eyewall interface is very similar to the IWRAP pass on 31 August 1400 UTC (see Figs. 4 and 5). The storm was in an intensifying state for both of these time periods, which indicates a connection between the larger, convective scales, which drive intensification, and the smaller, CTS scales. In the 4 September 2150 UTC pass, the native scales of the CTSs are ∼1.5–2 km at $r = \sim$38 km (see Fig. 9), which are connected with the individual, tall turbulent eddies observed in Fig. 8. These eddies are very similar to those observed on 3 September 0950 UTC (see Figs. 6 and 7) in a similar radial location. Finally, the wavelet image for the 5 September 0100 UTC pass (IWRAP data also averaged between 0.50 and 0.75 km height) shows a dominant region of power between $r = \sim$45 and 50 km with wavelengths between ∼2 and 4 km. This region contains short, but intense eddies (see Fig. 8) on top of a more diffuse background wind field as opposed to the concentrated, high wind speed regions observed in the previous radial legs.

The first C-band SAR image obtained for the Hurricane Dorian case (29 August at 1021 UTC) is shown in Fig. 10 on a storm-centered grid. The image covers a large portion of the storm circulation with the eyewall of the system well-placed near the image center. As expected, the VH NRCS intensity scales with the typical hurricane wind profile with minimum values in the eye (∼−32 dB), maximum values in the eyewall (∼−20 dB), and a slow roll-off with increasing radius to values of ∼−28 dB in the far field outside of rainband activity. Small-scale oscillations in the NRCS are visible throughout the image extending from the eyewall ($r = \sim$8–10 km) out to the edges of the image ($r = \sim$60 km). These oscillations are of interest here as they reflect variations in the surface wind stress, which are likely connected to some degree with features at higher levels in the boundary layer, as discussed in Section I.

Fig. 11 shows the perturbation NRCS from the three radial segments selected from the SAR image shown in Fig. 10. The perturbation data represent the scales from ∼5 km and below, as described in Section III-B. The maximum perturbation NRCS is located in the eyewall at $r = \sim$8 km, which is near the RMW at this time. Inside of this radius, there are some interesting perturbation signals located at the eye/eyewall interface. For example, in the blue curve labeled "radial 1" (azimuth of 38°), there is a perturbation NRCS signal at $r = 4$–5 km that appears reminiscent of eye/eyewall mixing events from mesovortices (e.g., [11]). Unfortunately, no supporting data from aircraft or satellite measurements were useful for examining this idea further. Thus, investigation of the eye/eyewall mixing hypothesis is left for future studies.

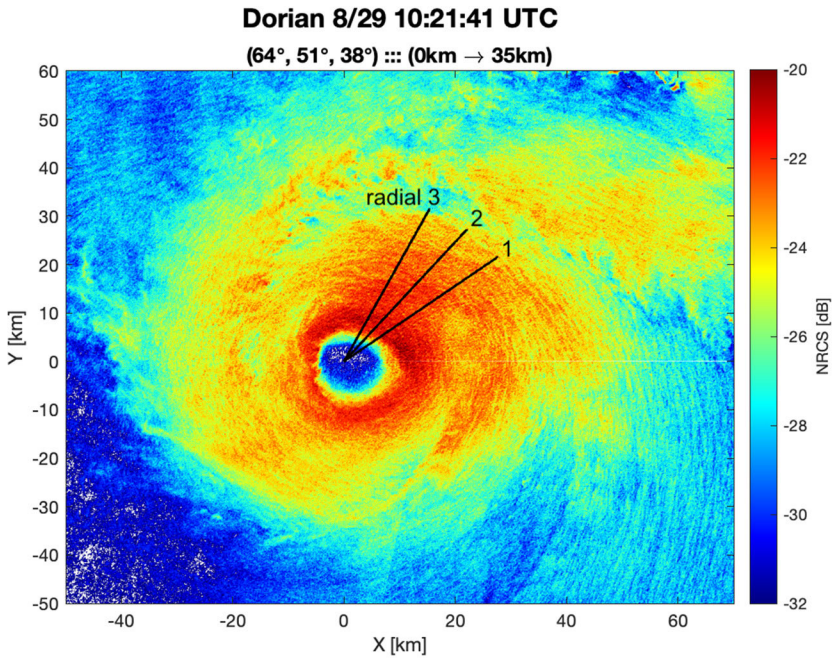

Fig. 10. C-band VH SAR image of Hurricane Dorian (2019) on 29 August at 1021 UTC with the ESA Sentinel-1B system. More details of the image can be found in Table I. The NRCS data in dB are placed on a storm-centered grid. The three black lines denote radials selected for wavelet analysis at various azimuths (64°, 51°, and 38° moving clockwise) extending from the storm center out to 35 km radius.

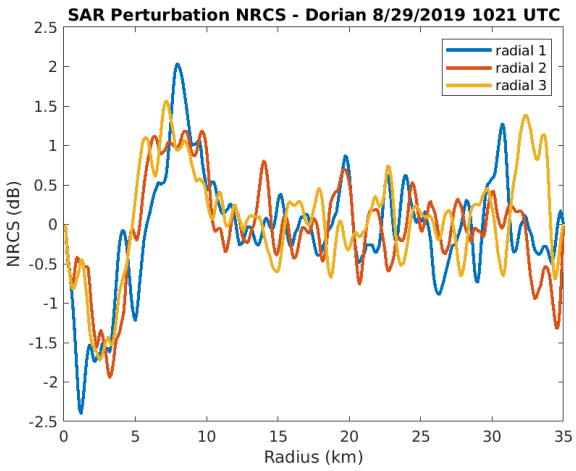

Fig. 11. Perturbation VH NRCS (dB) for the three radial segments shown by black lines in the SAR image shown in Fig. 10. The lines labeled "radial 1," "radial 2," and "radial 3" denote azimuths 38°, 51°, and 64°, respectively. See Fig. 10 for the locations of these radials.

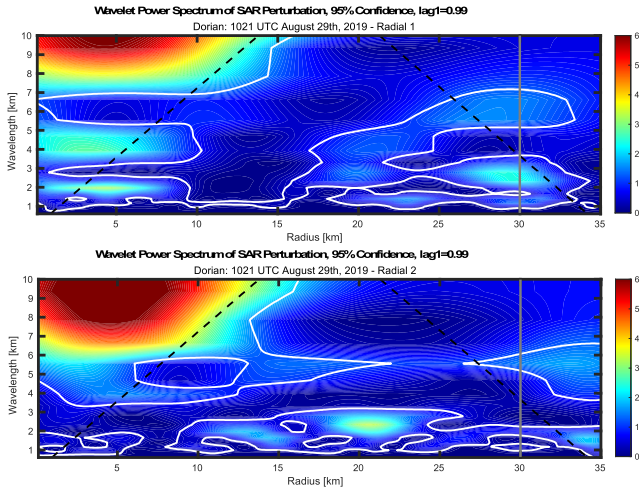

Fig. 12. Wavelet images corresponding to the perturbation VH NRCS data (see Fig. 11) sampled from the SAR image shown in Fig. 10. The panels show normalized power for (top) radial 1 and (bottom) radial 2. All other shown markings are the same as in Fig. 5.

The IWRAP data analysis has illustrated that wind speed perturbations at the eye/eyewall interface are out of phase with the peak precipitation. As a result, the precipitation noise in the SAR NRCS is reduced at the eye/eyewall interface, allowing a more direct connection to the wind speed signal. Outside of the broad peak in the eyewall, oscillations in the NRCS at $r > 10$ km show values of $\pm\sim 0.75$ dB that reflect the striations observed in the SAR image (see Fig. 10).

The perturbation NRCS radials are fed into the wavelet analysis and two of these wavelet images are analyzed here, which are sufficient to characterize the main features. Fig. 12 shows that for both radials, the peak power (>6) occurs at ~8–10-km wavelength in the radial region between ~0 and 10 km. This region reflects the broad scales associated with the eye and eyewall of the system that contain most of the energy. In radial 1, another significant peak in power (~3) is observed just downscale from the eye/eyewall with wavelengths centered at ~4.5 km in the $r = 0$–7 km range. This region is associated with the strong perturbations at the eye/eyewall interface, which also contains a secondary peak in power (~3–4) at wavelengths of 2 km. These distinct peaks in power are not apparent in radial 2, suggesting that these perturbations are confined azimuthally. The multiscale structure in radial 1, with similar wavelengths in the eyewall

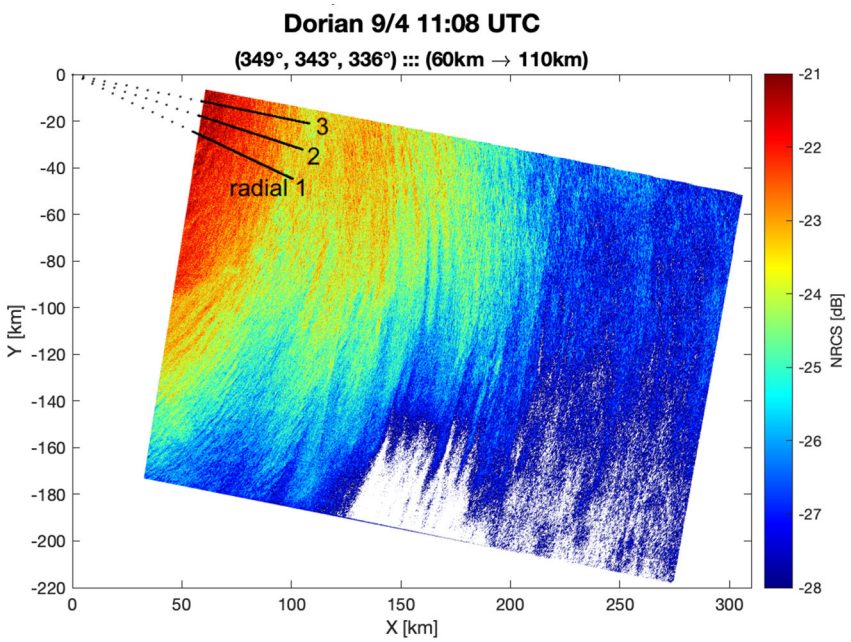

Fig. 13. C-band VH SAR image of Hurricane Dorian (2019) on 4 September at 1108 UTC with the ESA Sentinel-1B system. More details of the image can be found in Table I. The NRCS data in dB are placed on a storm-centered grid. The three black lines denote radials selected for wavelet analysis at various azimuths (349°, 343°, and 336° moving clockwise) extending from $r = 60$ to 110 km.

and at the eye/eyewall interface, was also evident in IWRAP data on August 31 at 1400 UTC (see Figs. 4 and 5) and on September 4 at 2150 UTC (see Figs. 8 and 9).

Outside of the eyewall ($r > 10$ km) in Fig. 12, both radials show significant peaks in power (∼2–3) in the 1–3-km wavelength range. It is difficult to determine whether these eddies are the same as those observed in IWRAP data just outside the eyewall, but the scales around 1–3 km are similar in both datasets.

Fig. 13 shows the second SAR image obtained for Dorian on 4 September at 1108 UTC. The overpass missed the inner core of the system, but quality data were obtained in the outer core region where oscillations in the NRCS are clearly visible throughout the image. Radial samples were chosen from the innermost radii to try and approximate the IWRAP data as best as possible, which resulted in segments from $r = 60$ to 110 km. The perturbation NRCS data along these three radial segments are shown in Fig. 14. The amplitude of the oscillations in the NRCS is ∼±0.75 dB, which is very similar to those documented in the previous SAR overpass (see Fig. 11) at outer radii.

The structure of the waves present in Fig. 14 is difficult to ascertain from the high-frequency oscillations, but the wavelet images help to pull out the dominant signals. As in the last SAR overpass, we only present the wavelet images for two radials here as this is sufficient to characterize the main features. The wavelet image for radial 1 (see Fig. 15), which is the bottom radial on the SAR image (see Fig. 13) at 336°, has two regions with peak power >6 centered at $r \sim 65$ km and $r \sim 95$ km. The center wavelength associated with these peaks is ∼5 km, which is right at the cutoff wavelength of the filter, but significant power is still present in these features at ∼3–4-km wavelength. In these same radial regions, secondary

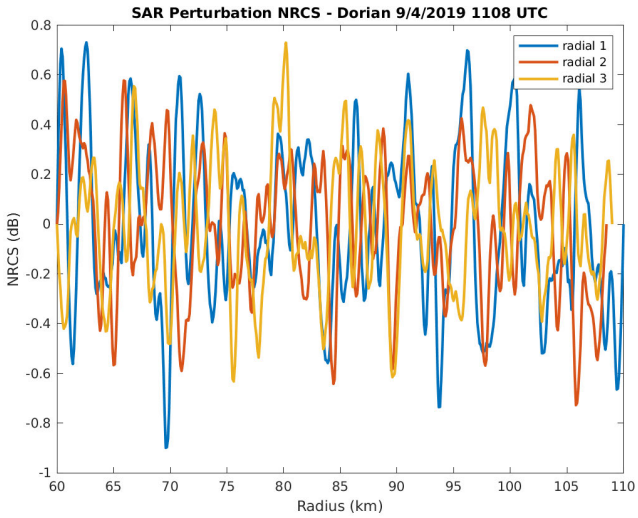

Fig. 14. Perturbation VH NRCS (dB) for the three radial segments shown by black lines in the SAR image shown in Fig. 13. The lines labeled "radial 1," "radial 2," and "radial 3" denote azimuths 336°, 343°, and 349°, respectively.

peaks in power are visible that have center wavelengths of ∼2 km. The power of these ∼2-km eddies is significantly larger at inner radii (60–70 km, power values > 6) than outer radii (85–105 km, power values ∼ 4), which may be tied to the stronger vertical wind shear present at inner radii [5], [8]. The wavelet image for radial 2 (see Fig. 15) also shows similar radial regions with peaks in power, but the power is more evenly distributed across scales starting from large scales (∼5–7 km) to medium scales (∼3–4 km) and down to small scales (∼1–2 km). This structure further elucidates the multiscale nature of the radar backscatter and,

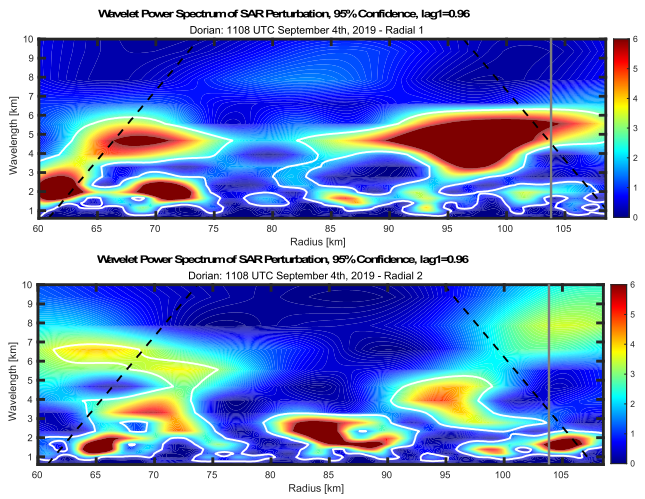

Fig. 15. Wavelet images corresponding to the perturbation VH NRCS data (see Fig. 14) sampled from the SAR image shown in Fig. 13. The panels show normalized power for (top) radial 1 and (bottom) radial 2. All other shown markings are the same as in Fig. 5.

by association, the surface wind field that is coupled to the turbulence structure in the boundary layer.

B. Composite Histograms

The following histograms represent the wavelengths of dominant turbulent features for all the Dorian and Rita data, separated by IWRAP and SAR results. The histograms are also stratified by features in the inner core ($r* <= 1.5$) and outer core ($r* > 1.5$). The Rita IWRAP data are shown elsewhere [8], [18], and the Rita SAR image is not shown for brevity due to the focus on the Dorian case. As a reminder, the histograms are built by selecting wavelengths from the wavelet images subject to the following constraints: 1) 95% confidence level anywhere within the wavelet image; 2) wavelength less than or equal to 5 km and greater than 1 km; and 3) radius less than the cutoff.

Figs. 16 and 17 show the composite eddy wavelength histograms for the IWRAP and SAR data, each split into inner core and outer core regions. The sample sizes in each individual composite are quite different, so we focus our discussion on the relative features of each group. In the IWRAP composites, there are two distinct modes present, ∼1 and ∼2 km, in the inner core and outer core groups despite the much larger counts in the inner core. For wavelengths greater than ∼2 km, there is a gradual decrease in counts with increasing wavelengths in both groups. The mean wavelengths for the inner core and outer core IWRAP data are almost identical (2.46 and 2.49 km, respectively). After accounting for the two distinct modes present in each group, a dominant wavelength of ∼2 km is an appropriate middle ground for the histogram statistics. This dominant scale is consistent with the features found in Guimond et al. [8] using IWRAP data.

A similar story is apparent in the SAR composites. In both the inner core and outer core groups, two distinct modes are present at ∼1 and ∼1.5 km, despite the outer core containing much larger counts. There are very few eddy wavelengths present at scales greater than ∼1.5 km in the inner core,

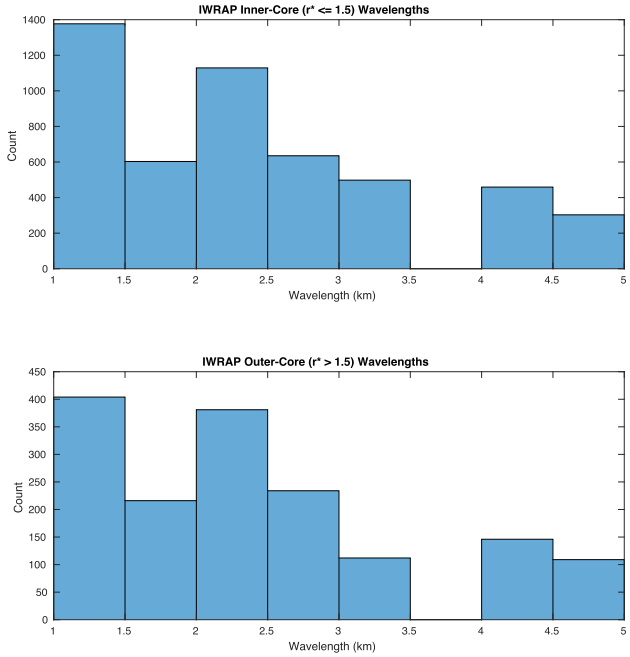

Fig. 16. Composite histograms for all IWRAP data showing CTS wavelengths from Hurricane Rita (2005) and Hurricane Dorian (2019). The mean and one standard deviation for the inner core and outer core histograms are 2.46 ± 1.11 and 2.49 ± 1.09 km, respectively.

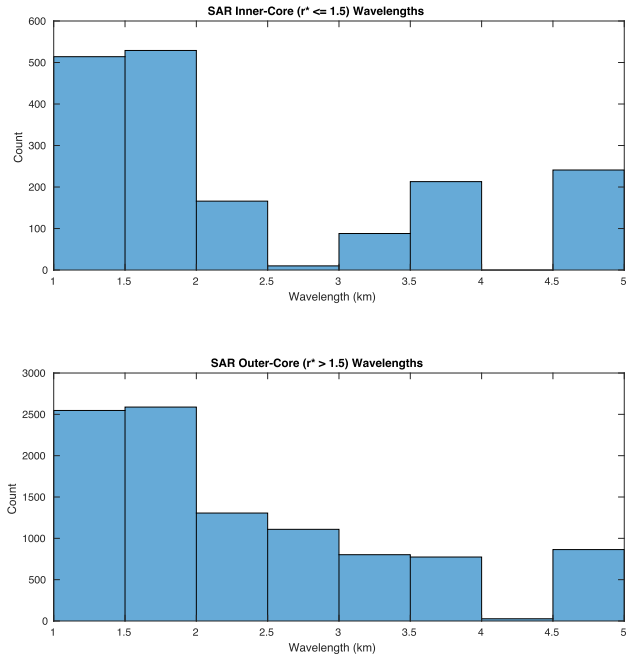

Fig. 17. Composite histograms for all SAR data showing CTS wavelengths from Hurricane Rita (2005) and Hurricane Dorian (2019). The mean and one standard deviation for the inner core and outer core histograms are 2.43 ± 1.24 and 2.38 ± 1.07 km, respectively.

but this group is only pulling from one SAR image. In the outer core, there is a steady decrease in counts with increasing wavelength beyond ∼1.5 km. This behavior is the same as that observed in the IWRAP composites. The inner core and outer core mean wavelengths are ∼2.43 and ∼2.38, respectively, which are only slightly smaller than the IWRAP values.

The commonalities in the CTS wavelength histograms between the IWRAP and SAR data are interesting. Both datasets show approximately lognormal probability density functions with similar dominant modes and mean wavelength values. Morrison et al. [15] also found lognormal distributions of turbulent eddy wavelengths in raw Doppler velocity data taken near landfalling hurricanes. Taking in the full scope of these statistics, the intrinsic scale of individual CTSs in both datasets is ∼2 km or perhaps slightly lower in the SAR data. The implications and applications of these findings for the study of the HBL are discussed in the next section.

V. Conclusions and Scientific Interpretation

The main goal of this article is to advance the understanding and documentation of the turbulent HBL, which is a critical region of these systems from both a scientific and societal point of view. Traditional wind measurements in the turbulent HBL rely heavily on Lagrangian point samples made by dropsondes and very limited radial legs of data made at one vertical level from aircraft or drones. While useful measurements, these data sources cannot provide the localized, 3-D structure of the HBL at the scales of large turbulent eddies. In this work, new remote sensing measurements of the turbulent HBL are examined through analysis of airborne (IWRAP) and spaceborne (SAR) radar data. The IWRAP measurements allow retrievals of the 3-D wind field to document and understand the structure of CTSs from flight level down to ∼150 m above the ocean surface. The grid spacing of the IWRAP 3-D wind fields is up to 125 m in the horizontal one (along track and across track) and 30 m in the vertical one. The SAR data provide important context for the localized IWRAP measurements by enabling wide swath views of the hurricane ocean surface at turbulence scales (∼100 m) through analysis of the NRCS. The IWRAP data, in turn, provide the detailed wind structure to interpret the ocean/atmosphere interface measured by the SAR.

A detailed case study of Hurricane Dorian (2019) was performed to analyze the CTSs present in the IWRAP and SAR data. For the radial legs shown here, the IWRAP data revealed peak wind speeds in the nadir plane of ∼65–75 m/s located inside CTSs near the eye–eyewall interface. These peak winds are often located at low levels (∼0.15–0.50 km), but sometimes they are found at much higher levels of ∼1.0–1.5 km, which is at or above the nominal boundary layer height of ∼1.0 km. The peak winds are found at these higher altitudes when the CTSs are vertically coherent, extending from the lowest levels (0.15 km) up to the ∼1.0–1.5-km layer. More research is needed to document the structure of these peak winds in the hurricane eyewall from various cases and explain how they are produced. Studies along these lines are currently being examined.

One SAR overpass of Dorian captured the inner core ($r < \sim 50$ km) of the system, including the eyewall. The NRCS measurements showed perturbations at the eye–eyewall interface that has some connections to the IWRAP CTSs described above. Wavelet analysis was performed on the IWRAP and SAR data to study the CTS wavelengths and power characteristics. The SAR data showed a multiscale structure in the wavelet power spectrum with peaks at ∼10 km (representing the eyewall), ∼4–5 km (representing a possible merger of small-scale eddies), and ∼2 km (the native scale of the CTSs). Several radial legs of IWRAP data showed a similar multiscale, three-peak structure with the native scale of individual CTSs around 2 km, a secondary peak at 3–4 km, and a larger scale maximum in power at 6–7 km.

Of particular interest is that the individual CTSs with a native scale of ∼2 km are occurring at the eye/eyewall interface where the radial shear of the tangential wind is largest. There are often a collection of several individual CTSs in this region that may combine to form the secondary peak in wavelet power near 3–4 km. Guimond et al. [8] analyzed IWRAP data in Hurricane Rita (2005) near peak intensity and during an eyewall replacement cycle and found similar results. The native scales of the CTSs were ∼2 km with the most intense eddy activity located on the inner edge of the outer eyewall with a shift to the inner edge of the inner eyewall after the replacement. The authors connected this eddy activity to the vertical shear of the radial and tangential wind. The current study suggests that the radial shear of the tangential wind should also be considered as an important source term for the instabilities and turbulence present in the HBL.

A second SAR overpass collected in the outer core ($r > \sim 50$ km) of Dorian also showed a peak in wavelet power at a scale of ∼2 km, representative of the intrinsic nature of the CTSs, all the way out to ∼100 km radius. However, the collocated triple peak in power observed in the inner core is not obvious in the outer core. This is likely a reflection of the different dynamics operating in these two regions. The inner core is characterized by persistent convection in the eyewall and large tangential winds with strong radial and vertical shear that can generate small-scale eddies. The superposition of these different scales produces multiple peaks in the wavelet power. The outer core contains more scattered convection and much weaker tangential winds with limited shear-induced eddies. Thus, the superposition of scales and associated multiple peaks in wavelet power is significantly reduced.

Composite histograms of CTS wavelengths from aggregated IWRAP and SAR data in Hurricane Rita (2005) and Hurricane Dorian (2019) were constructed to gauge the similarities and differences in the eddies contained in each dataset. The histograms were also stratified by features in the inner core ($r* <= 1.5$) and outer core ($r* > 1.5$). While the different sample sizes in each subgroup made direct comparisons challenging, some key takeaway messages are still clear. The dominant wavelength in all composites (regardless of data type) is ∼2 km, which appears associated with the intrinsic scale of individual CTSs as noted above for the case study of Dorian. This finding links the scale of CTSs from the ocean surface, through the boundary layer and entering into the free atmosphere near the top of the IWRAP sampling domain. This result was also found by Guimond et al. [8], but the addition of a new storm case (Dorian) and different dataset (SAR) is useful for generalizing the results.

The information described above can be used in numerical model turbulence parameterization schemes where free

parameters that describe the dominant length scale of large turbulent eddies are needed. The results from this article indicate that ∼2 km is an appropriate scale to use in these schemes. Note that the CTS wavelengths documented in this current article are significantly larger than some observational studies of boundary layer rolls (e.g., [14]), and Guimond et al. [8] highlight some potential reasons for these differences.

The superposition of several energetic scales in the inner core boundary layer, as highlighted by IWRAP and SAR data, indicates that substantial wave–wave nonlinear interactions are occurring. While this is not surprising for such a highly dynamic region, the documentation of the dominant scales associated with these interactions is useful and can motivate idealized numerical simulations or calculations with observational data. Sroka and Guimond [18] computed the eddy kinetic energy budget for the large-scale waves in the HBL using IWRAP data and found that the CTSs contributed ∼30% to the local time tendency. Further study of these interactions is warranted and the combination of IWRAP and SAR data could be used to provide input for idealized calculations along these lines. Ongoing work is focused on the kinematic signatures of the CTSs as well as their detailed dynamics and will be reported in due course.

ACKNOWLEDGMENT

The authors thank the flight crew of N42RF, especially Mike Mascaro and flight directors Jack Parrish and Mike Holmes, as well as the logistical and technical support of the NOAA Aircraft Operations Center (AOC), Lakeland, FL, USA. The scientific results and conclusions, as well as any views or opinions expressed herein, are those of the author(s) and do not necessarily reflect those of NOAA or the Department of Commerce. Finally, they thank two anonymous reviewers for their extensive feedback that significantly improved the quantitative results of this article.

REFERENCES

[1] S. Aberson, M. T. Montgomery, M. Bell, and M. Black, "Hurricane Isabel (2003): New insights into the physics of intense storms. Part II: Extreme localized wind," *Bull. Amer. Meteorolog. Soc.*, vol. 87, no. 10, pp. 1335–1348, Oct. 2006.

[2] J. R. Carswell, D. Perkovic, T. Chu, S. J. Frasier, P. Chang, and Z. Jelenak, "Preliminary investigation of splash effect on high wind C-band HH-pol model function," in *Proc. IEEE Int. Geosci. Remote Sens. Symp.*, Jul. 2010, pp. 2539–2542, doi: 10.1109/IGARSS.2010.5651890.

[3] Y. Du and P. W. Vachon, "Characterization of hurricane eyes in RADARSAT-1 images with wavelet analysis," *Can. J. Remote Sens.*, vol. 29, no. 4, pp. 491–498, Jan. 2003.

[4] D. E. Fernandez et al., "IWRAP: The imaging wind and rain airborne profiler for remote sensing of the ocean and the atmospheric boundary layer within tropical cyclones," *IEEE Trans. Geosci. Remote Sens.*, vol. 43, no. 8, pp. 1775–1787, Aug. 2005.

[5] R. C. Foster, "Why rolls are prevalent in the hurricane boundary layer," *J. Atmos. Sci.*, vol. 62, no. 8, pp. 2647–2661, Aug. 2005.

[6] J. L. Franklin, M. L. Black, and K. Valde, "GPS dropwindsonde wind profiles in hurricanes and their operational implications," *Weather Forecasting*, vol. 18, no. 1, pp. 32–44, Feb. 2003.

[7] S. R. Guimond, L. Tian, G. M. Heymsfield, and S. J. Frasier, "Wind retrieval algorithms for the IWRAP and HIWRAP airborne Doppler radars with applications to hurricanes," *J. Atmos. Ocean. Technol.*, vol. 31, no. 6, pp. 1189–1215, Jun. 2014.

[8] S. R. Guimond, J. A. Zhang, J. W. Sapp, and S. J. Frasier, "Coherent turbulence in the boundary layer of Hurricane Rita (2005) during an eyewall replacement cycle," *J. Atmos. Sci.*, vol. 75, no. 9, pp. 3071–3093, Sep. 2018.

[9] S. R. Guimond, S. Sroka, and D. Protzko, "A large eddy simulation of hurricane intensification," in *Proc. 33rd Conf. Hurricanes Tropical Meteorol.* Boston, MA, USA: American Meteorological Society, May 2018, p. 17. [Online]. Available: https://ams.confex.com/ams/33HURRICANE/webprogram/Manuscript/Paper339570/large_eddy_33hurr_guimond.pdf

[10] K. B. Katsaros, P. W. Vachon, P. Black, P. D. Dodge, and E. Uhlhorn, "Wind fields from SAR: Could they improve our understanding of storm dynamics?" *Johns Hopkins Apl Tech. Dig.*, vol. 21, no. 1, pp. 86–93, Jan. 2000. [Online]. Available: http://www.jhuapl.edu/techdigest/TD/td2101/katsaros.pdf

[11] J. P. Kossin and M. D. Eastin, "Two distinct regimes in the kinematic and thermodynamic structure of the hurricane eye and eyewall," *J. Atmos. Sci.*, vol. 58, no. 9, pp. 1079–1090, May 2001.

[12] X. Li et al., "Tropical cyclone morphology from spaceborne synthetic aperture radar," *Bull. Amer. Meteorolog. Soc.*, vol. 94, no. 2, pp. 215–230, Feb. 2013.

[13] Y. Liu, X. S. Liang, and R. H. Weisberg, "Rectification of the bias in the wavelet power spectrum," *J. Atmos. Ocean. Technol.*, vol. 24, no. 12, pp. 2093–2102, Dec. 2007, doi: 10.1175/2007JTECHO511.1.

[14] S. Lorsolo, J. L. Schroeder, P. Dodge, and F. Marks, "An observational study of hurricane boundary layer small-scale coherent structures," *Monthly Weather Rev.*, vol. 136, no. 8, pp. 2871–2893, Aug. 2008, doi: 10.1175/2008MWR2273.1.

[15] I. Morrison, S. Businger, F. Marks, P. Dodge, and J. A. Businger, "An observational case for the prevalence of roll vortices in the hurricane boundary layer," *J. Atmos. Sci.*, vol. 62, no. 8, pp. 2662–2673, Aug. 2005, doi: 10.1175/JAS3508.1.

[16] J. Sapp, Z. Jelenak, P. Chang, and S. J. Frasier, "C-band cross-polarization airborne ocean surface NRCS observations in hurricanes: 2015–2019," in *Proc. IEEE Int. Geosci. Remote Sens. Symp.*, Sep. 2020, pp. 5647–5650.

[17] J. W. Sapp, S. O. Alsweiss, Z. Jelenak, P. S. Chang, S. J. Frasier, and J. Carswell, "Airborne co-polarization and cross-polarization observations of the ocean-surface NRCS at C-band," *IEEE Trans. Geosci. Remote Sens.*, vol. 54, no. 10, pp. 5975–5992, Oct. 2016, doi: 10.1109/TGRS.2016.2578048.

[18] S. Sroka and S. R. Guimond, "Organized kinetic energy backscatter in the hurricane boundary layer from radar measurements," *J. Fluid Mech.*, vol. 924, p. A21, Oct. 2021.

[19] C. Torrence and G. P. Compo, "A practical guide to wavelet analysis," *Bull. Amer. Meteorolog. Soc.*, vol. 79, no. 1, pp. 61–78, Jan. 1998.

[20] J. A. Zhang, K. B. Katsaros, P. G. Black, S. Lehner, J. R. French, and W. M. Drennan, "Effects of roll vortices on turbulent fluxes in the hurricane boundary layer," *Boundary-Layer Meteorol.*, vol. 128, no. 2, pp. 173–189, Aug. 2008.

[21] Z. Zhang and J. C. Moore, "Improved significance testing of wavelet power spectrum near data boundaries as applied to polar research," *Adv. Polar Sci.*, vol. 22, no. 3, pp. 192–198, Sep. 2011, doi: 10.3724/SP.J.1085.2011.00192.

Devin E. Protzko received the B.S. degree in physics and mathematics from the Physics Department, University of Maryland Baltimore County, Baltimore, MD, USA, in 2020.

Currently, he is a Research Scientist with the Optics and Photonics Group, Johns Hopkins University Applied Physics Laboratory, Laurel, MD, USA, where he primarily prototypes, fields, and analyzes various radiometric and spectroscopic diagnostics. He has interest/experience in geophysical fluid modeling and large-scale simulations of boundary layer interactions, as well as professional interest/experience in applied spectroscopy, material characterization, and remote sensing.

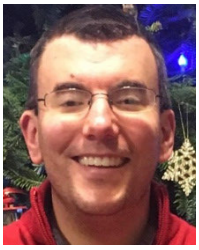

Stephen R. Guimond received the B.S. degree from Iowa State University, Ames, IA, USA, in 2004, and the M.S. and Ph.D. degrees from Florida State University, Tallahassee, FL, USA, in 2007 and 2010, respectively, all in atmospheric science.

From 2010 to 2012, he was a NASA Post-Doctoral Fellow with the NASA Goddard Space Flight Center (GSFC), Greenbelt, MD, USA. Currently, he is an Associate Professor with the Department of Atmospheric and Planetary Sciences, Hampton University, Hampton, VA, USA. His research interests are in radar remote sensing and geophysical fluid dynamics. The remote sensing work has a focus on airborne Doppler radar, including designing algorithms for computing geophysical variables such as winds, latent heat, and precipitation. The geophysical fluid dynamics work has a focus on hurricanes, convection, turbulence, and computational methods.

Christopher R. Jackson received the M.S. degree in applied physics from George Mason University, Fairfax, VA, USA, in 1998.

He is currently the Chief Scientist of Global Ocean Associates, Alexandria, VA, USA. His current activities include supporting the Center for Satellite Applications and Research (STAR), the National Environmental Satellite, Data and Information Service (NESDIS), and the National Oceanic and Atmospheric Administration (NOAA). His work there includes research and development in synthetic aperture radar remote sensing of the ocean surface across a range of phenomena (ocean surface winds, tropical cyclone winds, sea ice characterization, and sea ice drift motions) with an emphasis on product development to support operational uses.

Mr. Jackson served as a Principal Editor for the *Synthetic Aperture Radar Marine User's Manual* (NOAA, 2004).

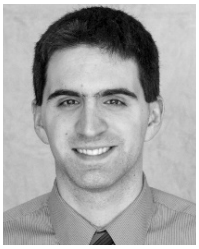

Joseph W. Sapp (Senior Member, IEEE) received the B.S. degree in electrical engineering from Pennsylvania State University, University Park, PA, USA, in 2006, and the Ph.D. degree in electrical and computer engineering from the University of Massachusetts at Amherst, Amherst, MA, USA, in 2015.

From 2006 to 2009, he was a Project Electrical Engineer with Lutron Electronics Company Inc., Coopersburg, PA, USA, during which he was involved in the embedded software design of multiple commercial products. In 2009, he joined the Microwave Remote Sensing Laboratory, University of Massachusetts at Amherst, to complete his graduate work. During this time, he had the opportunity to begin participating in flights with the National Oceanic and Atmospheric Administration (NOAA) Hurricane Hunters. Since 2015, he has been with the NOAA/National Environmental Satellite, Data and Information Service (NESDIS)/Center for Satellite Applications and Research (STAR), College Park, MD, USA, as a Support Scientist with Global Science and Technology, Inc., Greenbelt, MD, USA. His recent research involves using active, passive, and in situ sensors together to improve the algorithms and equipment used in remote sensing of ocean surface and atmospheric wind vectors in extreme environments.

Zorana Jelenak (Member, IEEE) received the Ph.D. degree in physics from Waikato University, Hamilton, New Zealand, in 2000.

Since 2001, she has been a Project Scientist with University Corporation for Atmospheric Research (UCAR) and a member of the Ocean Winds Team, National Oceanic and Atmospheric Administration (NOAA)/National Environmental Satellite, Data and Information Service (NESDIS)/Center for Satellite Applications and Research (STAR), College Park, MD, USA. Her research interests are in ocean remote sensing from active and passive microwave airborne and spaceborne instruments, with an emphasis on ocean wind and wave measurements. Of particular interest is data applicability in an operational near-real-time environment, retrieval algorithm development, model function development, and advanced statistical analysis and error analysis for improved product and retrieval algorithm characterization.

Paul S. Chang (Senior Member, IEEE) received the Ph.D. degree in electrical engineering from the University of Massachusetts at Amherst, Amherst, MA, USA, in 1994.

Since 1994, he has been a Research Physical Scientist with the Center for Satellite Applications and Research, National Environmental Satellite, Data and Information Service (NESDIS), National Oceanic and Atmospheric Administration (NOAA), College Park, MD, USA. Current activities include research and development in active and passive microwave remote sensing of the ocean surface with an emphasis on retrieval of the ocean surface wind field. Wind retrieval algorithm improvements and new product developments are pursued through the analyses of satellite and aircraft microwave remote sensing data. An emphasis is placed on transitioning research results into operational use, which involves cooperative relationships with the operational facets of NESDIS and with the National Weather Service, a primary end user of this data.